

Photodesorption by resonant laser-vibrational coupling: Effects of coherent two-quantum transitions, vibrational anharmonicity, and surface heterogeneity on yields

Z. W. Gortel, P. Piercy, and R. Teshima

Department of Physics, University of Alberta, Edmonton, Alberta, Canada T6G 2J1

H. J. Kreuzer

Department of Physics, Dalhousie University, Halifax, Nova Scotia, Canada B3H 3J5

(Received 15 September 1986)

Photodesorption may be initiated by resonant, laser-induced excitation of an internal vibrational mode of an adsorbed molecule. The desorption kinetics are predicted from a quantum-statistical theory based on a master equation describing phonon- and photon-assisted molecular transitions as well as elastic tunneling processes. Explicit contributions to desorption by coherent two-phonon and by one-photon-plus-one-phonon absorption and emission are shown to be important, while coherent two-photon processes are typically negligible. The calculated line shape of the photodesorption yield can differ from the corresponding infrared absorption spectrum due to nonlinear intensity effects, vibrational anharmonicity, and surface heterogeneity. A qualitative comparison with published experimental results on the adsorption systems CH_3F on NaCl , pyridine on KCl , and Co and NaCl is presented.

I. INTRODUCTION

Photodesorption of physisorbed molecules can be induced by resonantly exciting an internal vibrational mode of the adsorbate with infrared laser radiation.^{1,2} Desorption from both insulating²⁻⁵ and metallic^{6,7} substrates has been observed experimentally. The desorption yield per incident laser pulse is found to increase nonlinearly with laser intensity and depends resonantly on the laser frequency. Theoretical studies⁸⁻¹² of the kinetics of this photodesorption process have been advanced. To model the photodesorption mechanism it is necessary to describe the interaction of an adsorbed molecule with both the laser radiation field and with the thermal motion (phonons) or the substrate. In a previous paper,¹² we calculated the intensity dependence of the photodesorption rate constant using a microscopic master equation to include incoherent sequences of one-photon and one-phonon absorption and emission and elastic vibrational to translational tunneling processes. This theory is now extended to include coherent two-phonon, two-photon, and one-photon-plus-one-phonon transitions¹³ in higher-order perturbation theory. In addition, the influence of anharmonicity of the internal vibrational mode on the desorption yield is studied here. Note that, in contrast, the full anharmonicity of the molecule-surface bond must be included in the theory from the beginning.¹² Finally, inhomogeneous vibrational line broadening is modeled and the frequency spectrum of the photodesorption yield is studied.¹⁴ The effects of resonant surface heating^{15,16} and of lateral vibrational energy transfer,^{17,18} considered previously, are only commented on here.

The importance of coherent multiphonon processes in thermal desorption has already been emphasized theoretically. Bendow and Ying¹⁹ and Gortel *et al.*²⁰ have calculated multiphonon contributions to the desorption rate

of an atom physisorbed in a shallow surface potential that develops a single bound state. The latter work shows that absorption of a single phonon dominates in the desorption rate provided the binding energy is less than the maximum phonon energy. On the other hand, two-phonon absorption is essential when the bound-state energy becomes greater than the maximum phonon energy. For more strongly bound adsorption systems developing many bound states, Jedrzejek *et al.*²¹ demonstrated the importance of a subset of coherent multiphonon contributions to the transition rates included in a master equation theory of thermal desorption. The inclusion of coherent multiphonon effects in photodesorption is therefore of interest.

Since the coupling between an adsorbed molecule and the phonon bath of the substrate is quite efficient, coherent absorption and emission of one phonon and one photon can enhance internal vibrational excitation in the photodesorption process. This process will contribute asymmetrically to the yield line shape. On the other hand, coherent two-photon absorption processes will be shown to be of negligible importance in the rapid dephasing limit, in agreement with Lin and Fain.^{8,9}

The internal vibrational anharmonicity of adsorbed molecules is typically of the same order of magnitude as the linewidth,²² and must therefore influence the photodesorption kinetics when higher vibrational levels are excited. This is seen in both the laser intensity dependence of the yields, as studied by Jedrzejek,²³ and in the photodesorption yield line shape discussed here.

However, the spectral dependence of the photodesorption rate depends not only on the homogeneous effects noted above, but also on inhomogeneous broadening of the vibrational line shape. Vibrational decay and dephasing processes together have been calculated to give homogeneous internal vibrational linewidths of the order of

$\approx 10 \text{ cm}^{-1}$.²³⁻²⁶ In addition, inhomogeneous line broadening is caused by heterogeneity due to different adsorption sites, surface imperfections, and by random partial coverage²⁷ leading to varying molecular environments on the surface. Inhomogeneous vibrational line broadening by up to 10 cm^{-1} is thus possible.²⁸ The corresponding effect on the photodesorption spectrum will be calculated in a master equation approach.

In Sec. II, the formulation of the photodesorption rate calculation is described, including the developments outlined above. Additional technical details may be found in Ref. 11. The dependence of the desorption rate on both laser intensity and frequency is shown in detail in Sec. III, for different adsorption systems. Finally, contact with experimental results is discussed, along with concluding remarks in Sec. IV.

II. THEORETICAL FORMALISM

In this section the model adsorption system and master equation approach to desorption kinetics are introduced. The Hamiltonian for the full, interacting solid + gas + laser system is then constructed, from which the transition rates are calculated.

To describe the statics of a molecule adsorbed on a solid surface we note that for the photodesorption process studied here, it is sufficient to consider only that vibrational mode of the molecule into which the laser is coupled. We therefore represent the molecule by a diatomic with fundamental frequency Ω and oscillator quantum number $v=0, 1, \dots, v_{\max}$; the latter is truncated since vibrational anharmonicity, included later, makes excitation beyond v_{\max} inefficient. Further we assume that the dynamic dipole of the molecule is perpendicular to the surface; tilting leads to an additional angular dependence of the photodesorption yield that has been studied in Ref. 12. The physisorption interaction between the gas molecule and the static solid is described by a one-dimensional surface potential $V_s(x_1)$ which develops discrete bound states of negative energy labeled $i=0, 1, \dots, i_{\max}$, and a continuum of gas-phase states of positive energy with wave vector q . Here x_1 is the distance between the close end of the molecule and the surface. The dynamic interaction between an adsorbed molecule, the laser radiation, and the phonons of the solid causes transitions $(i, v) \rightarrow (i', v')$ between states of both molecular translational motion (i) in the surface potential and internal vibrational motion (v), with probability per unit time $R_{v'i}^{v'v}$. Desorption occurs when a molecule, adsorbed in some bound state i of the surface potential makes a transition to a continuum state.

The calculation of the photodesorption rate is based on the master equation¹²

$$\begin{aligned} \frac{d}{dt} n_i^v(t) = & \sum_{i', v'} R_{ii'}^{vv'} n_{i'}^{v'}(t) - \sum_{i', v'} R_{i'i}^{v'v} n_i^v(t) \\ & - \sum_{v'} (P_{ci}^{v'v} + Q_{ci}^{v'v}) n_i^v(t), \end{aligned} \quad (1)$$

describing the evolution of the occupation probability $n_i^v(t)$ of the (i, v) state. The first two terms in (1)

represent bound-state to bound-state transitions in the surface potential, while the third term describes bound-to-continuum-state transitions that deplete the adsorbate population. The master equation (1) is usually derived from the Liouville equation for the adsorbate (dynamic subsystem) interacting with phonons and electromagnetic radiation (dissipative subsystems).⁸ A number of approximations are invoked in this derivation: (i) one assumes that the process is Markovian, i.e., the relaxation time of the dynamic subsystem T_0 is long in comparison with the lifetime τ_c of correlations building up in it due to its interaction with the dissipative subsystems. (ii) The separations $|E_i^v - E_{i'}^{v'}|/\hbar$ between the energy levels of the adsorbate are assumed to be large in comparison with T_0^{-1} and with the frequency of microscopic transitions between the levels. The latter condition may be violated in some cases for densely spaced levels near the top of the surface potential well. The perturbation theory, used to compute the transition probabilities (1), breaks down for the same levels, as discussed in Secs. II B and III.

The desorption rate r_d is equal to the rate of depopulation of the bound states (i) and is given by

$$r_d = - \frac{\frac{d}{dt} \sum_{i,v} n_i^v(t)}{\sum_{i,v} n_i^v(t)} \quad (2)$$

and may be determined numerically solving the coupled system of rate equations (1) for initial conditions of thermal equilibrium.²⁹ It turns out that, in most cases, the desorption kinetics is describable by a single time scale, given by the smallest eigenvalue λ_0 of the rate matrix in (1),¹² so that $r_d = \lambda_0$. Furthermore, the laser pulse time t_L used experimentally is typically much shorter than the desorption time r_d^{-1} . The photodesorption yield Y per laser pulse is then given by¹⁶

$$Y \approx N r_d t_L \quad \text{for } r_d t_L \ll 1, \quad (3)$$

where N is the number of adsorbed molecules within the spot on the surface irradiated by the laser.

A. Hamiltonian

The Hamiltonian of the gas-solid-laser system is now constructed in second quantized form, in analogy with Ref. 12. The interaction potential $V(x_1)$ between a gas molecule and the static solid, along with the internal vibrational potential of the molecule, together lead to the static Hamiltonian¹²

$$H_{\text{st}} = H_0 + H_{\text{res}}. \quad (4)$$

Here H_0 describes independent internal vibrational (v) and molecular-center-of-mass translational (i) modes with energy eigenvalues $E_i^v = E_i + E_v$, and annihilation operator α_j^v , so that

$$H_0 = \sum_{i,v} E_i^v \alpha_i^v \dagger \alpha_i^v. \quad (5)$$

Choosing $V(x_1)$ to be a one-dimensional Morse potential in the direction normal to the surface, the eigenvalues E_i

and corresponding eigenvectors of overall molecular translational motion are analytically calculated.²⁹ The energy level spacing of the internal vibrational mode, with a small anharmonic energy shift Δ included, is given by

$$E_{v+1} - E_v = \hbar(\Omega - v\Delta). \quad (6)$$

For the low-lying states $v=0,1,2, \dots$ considered here.

However, the translational and internal vibrational modes perpendicular to the surface are coupled by the second term H_{res} in (4). This interaction is due to the dependence of the surface potential energy $V(x_1)$ on the position x_1 of the end of the (diatomic) molecule closest to the surface, which is in turn dependent on both the vibrational and translational (center-of-mass) coordinates x and ξ , respectively, according to $x_1 = x - \mu/m_1\xi$. (μ and m_1 are the reduced mass and mass of the nearer end, respectively, of the adsorbed diatomic molecule.)

The dynamic interaction of the adsorbed molecule with the laser radiation and thermal motion of the substrate are contained in the interaction Hamiltonian

$$H_{\text{int}} = H_l + H_{\text{ph}}. \quad (7)$$

Here,

$$H_l = \int dx \int d\xi \psi^\dagger(x, \xi) \left[-i\hbar \frac{Q}{\mu} A(x, t) \frac{\partial}{\partial \xi} \right] \psi(x, \xi) \quad (8)$$

describes the interaction of the internal molecular vibrational mode with the laser radiation, in second quantized form. The quantity in the large parentheses represents the minimal coupling³⁰ Hamiltonian; Q is an effective charge.

The electromagnetic field due to the laser radiation in the presence of the surface is described by the vector potential $\mathbf{A}(\mathbf{x}, t)$. For infrared wavelengths, the potential is essentially uniform over atomic dimensions, so that the component perpendicular to the surface may be approximated as

$$\begin{aligned} A(\mathbf{x}, t) &\cong A(0, t) \\ &= \left[\frac{\hbar}{2\epsilon_0} \right]^{1/2} \sum_k \Omega_k^{-1/2} \mathbf{n} \cdot \mathbf{U}_k(0) [c_k^\dagger(t) + c_k(t)]. \end{aligned} \quad (9)$$

Here $\mathbf{U}_k(\mathbf{x})$ is the normal mode of the radiation field at the surface with incident wave vector and polarization $k = (\mathbf{k}, \beta)$, given explicitly in Ref. 12, and \mathbf{n} is a unit vector normal to the surface. The corresponding annihilation operator is $c_k(t)$, the mode frequency is Ω_k , and ϵ_0 is the permittivity of free space.

The quantized molecular field operator $\psi(x, \xi)$ in (8) may be expanded in terms of the one-dimensional eigenfunctions $\phi_i(x)$ and $u_v(\psi)$ of the Morse surface potential and harmonic vibration mode, respectively, giving

$$\psi(x, \xi) = \sum_{i,v} \phi_i(x) u_v(\xi) \alpha_i^\dagger(t) \alpha_i^v(t). \quad (10)$$

The interaction between the adsorbed molecule and thermal phonons of the solid is given by H_{ph} in (7) which takes the form

$$\begin{aligned} H_{\text{ph}} &= \int dx \int d\xi \psi^\dagger(x, \xi) [V(x - (\mu/m_1)\xi - a(t)) \\ &\quad - V(x - (\mu/m_1)\xi)] \psi(x, \xi). \end{aligned} \quad (11)$$

The dynamic surface displacement $a(t)$ at the site of the adsorbed molecule is expanded in terms of the phonon modes of an infinite solid to get

$$a(t) = \left[\frac{\hbar}{2M_s N_s} \right]^{1/2} \sum_P \frac{\hat{\mathbf{e}}_p \cdot \mathbf{n}}{w_p^{1/2}} [b_p^\dagger(t) + b_p(t)], \quad (12)$$

where $\hat{\mathbf{e}}_p$, w_p , and $b_p(t)$ are the polarization vector, frequency, and annihilation operator, respectively, of the phonon mode with wave vector and polarization $p = (\mathbf{p}, \sigma)$. In (12), M_s is the mass of a unit cell of the solid, N_s is the number of such cells. This formula ignores the presence of surface phonon modes, which would enhance the coupling somewhat but do not change the results qualitatively.³¹ Furthermore, lateral variation of $a(t)$ along the surface is neglected here, as is appropriate at low temperatures for which long-wavelength phonon displacements dominate in (12).

The potential energy difference due to surface motion [square brackets in (11)] may be expanded in powers of the phonon field amplitude $a(t)$ as

$$\begin{aligned} &V(x - (\mu/m_1)\xi - a(t)) - V(x - (\mu/m_1)\xi) \\ &= -a(t) \frac{\partial}{\partial x} V(x - (\mu/m_1)\xi) \\ &\quad + \frac{1}{2} a^2(t) \frac{\partial^2}{\partial x^2} V(x - (\mu/m_1)\xi) + \dots \end{aligned} \quad (13)$$

Whereas the first term only was included in our previous work,¹² the second term contributes to coherent two-phonon transitions. The interaction Hamiltonian (7) is now used to calculate the molecular transition rates.

B. Transition rates

The single molecule transition rate from state $(i, v) \rightarrow (i', v')$ is defined as the time derivative of the corresponding transition probability, taken at long times.¹¹ Thus

$$R_{i'v'}^{iv} = \lim_{t \rightarrow \infty} \left[\frac{d}{dt} \text{Tr} \left[\langle iv | U^\dagger(t) | i'v' \rangle \langle i'v' | U(t) | iv \rangle \rho_s \rho_l \right] \right], \quad (14)$$

where the evolution operator $U(t)$ is given in the sudden approximation by

$$U(t) = T \exp \left[\frac{1}{i\hbar} \int_0^t d\tau H_{\text{int}}(\tau) \right] \quad (15)$$

using the Wick time-ordering operator T . The trace operation in (14) runs over all phonon states of the solid and laser photon states. The initial-time density matrices of the phonons and photons are ρ_s and ρ_l , respectively.

By keeping ρ_s and ρ_l constant (and diagonal) throughout the desorption process, Markovian behavior is assumed.

To evaluate the transition rate (14), the evolution operator $U(t)$ is expanded in powers of H_{int} . The first-order terms simply give Fermi's golden rule formula,³² which was exploited previously.¹² However, the many-particle phonon and photon states involved in the trace operation in (14) make higher-order terms in a direct expansion of $U(t)$ quite complicated. To overcome this problem, we adopt the methods of thermo field dynamics³³ (TFD) to describe the phonon and photon systems. This approach is advantageous over the more conventional techniques of thermal field theory³⁴ because it is compatible with our time-dependent formalism and is also capable of describing the nonthermal photon states of the laser radiation.

Using the theory of TFD, averaging over the states of the phonon and photon reservoirs is accomplished by taking an expectation value given by

$$\text{Tr}_{s,l}[B(t)\rho_s\rho_l]=\langle\beta|\langle I|B(T)|I\rangle|\beta\rangle. \quad (16)$$

The operator $B(t)$ is an arbitrary function of the phonon and photon amplitudes. It is averaged by taking its expectation value in the "thermal phonon ground state" $|\beta\rangle$ of the solid, and in the "photon ground state" $|I\rangle$ of the laser radiation. The former is characterized by the inverse temperature β of the solid, while the latter depends on the intensity distribution I_k of the laser radiation. The information stored in the reservoir density matrices ρ_s and ρ_l is now contained in the states $|\beta\rangle$ and $|I\rangle$, respectively. The field operators for which $|\beta\rangle$ and $|I\rangle$ are ground states are related to the original phonon and photon fields by unitary transformations,³³ also see Ref. 11 for more details.

Substituting (16) into (14), inserting the identity operator in the reservoir's state space, and doing the time derivative leads to

$$R_{i'v'}^{v'v} = \sum_{n_s(\beta)} \sum_{n_l(I)} \langle n_l(I), n_s(\beta), i'v' | U(\infty) | iv\beta, I \rangle \left\langle n_l(I), n_s(\beta), i'v' \left| U(\infty) \frac{H_{\text{int}}(0)}{i\hbar} \right| iv, \beta, I \right\rangle^* + \text{c.c.} \quad (17)$$

Here, $n_s(\beta)$ and $n_l(I)$ run over excited phonon and photon states, measured with respect to the thermal phonon and photon ground state, $|\beta\rangle$ and $|I\rangle$, respectively.¹¹ The sum over $n_s(\beta)$ and $n_l(I)$ above enables us to classify contributions to $R_{i'v'}^{v'v}$ in terms of one- and two-phonon absorption or emission processes, and so on. The matrix elements in (17) thus involve at most few-particle phonon-photon states. As a result, a standard Feynman diagram expansion^{34,11} of the transition amplitudes in (17) is now practical.

The diagrammatic expansion of (17) permits calculation of coherent, many-phonon(photon)-absorption and emission processes, along with self-energy and vertex corrections. However, a finite long-time transition rate can only be calculated for sharp initial and final states.^{32,35} This restriction means neglecting self-energy corrections in the initial and final states, and reduces (17) to¹¹

$$R_{i'v'}^{v'v} = \sum_{n_s(\beta)} \sum_{n_l(I)} \frac{2\pi}{\hbar^2} |\langle n_l(I), n_s(\beta), i'v' | U(\infty) H_{\text{int}}(0) | iv, \beta, I \rangle|^2 \delta(\epsilon_{i'}^{v'} - \epsilon_i^v + \epsilon_l + \epsilon_s). \quad (18)$$

The four terms within the Dirac δ function are, in order, the energies (divided by \hbar) of the molecular final and initial states and the final photon and phonon states.

In the calculation that follows, transition rates involving the real absorption and/or emission of one or two phonons are considered, as shown in Fig. 1. Vertex corrections are neglected, but self-energy (linewidth) corrections are included in the intermediate molecule-state Green's functions that appear in the two-vertex processes. This reflects the fact that intermediate molecular states are, in reality, not discrete but in fact quasistationary.³⁵ Without the inclusion of intermediate state linewidths, a finite long-time transition rate cannot be obtained. The transition rate formula (18) is, in these approximations, equivalent to the usual T -matrix approach described, for example, by Messiah,³² for resonance scattering.

The "long-time limit" taken in Eq. (14) for the transition rate can now be quantified. We must consider times large on the scale of the inverse molecular linewidth, but short compared to the transient evolution time scale given by the vibrational lifetime. This corresponds to taking $t \rightarrow \infty$ in (14). Note, however, that since the surface bound states (i) are primarily lifetime broadened, a con-

ventional rapid dephasing approximation is inapplicable here.

The specific transition rates entering the master equation can now be derived. The first-order contributions in (18), obtained by approximating $U(\infty)=1$, lead to the Fermi golden rules rates calculated in Ref. 12. The transition rate $R_{i'v'}^{v'v}$ in the master equation (1) receives both

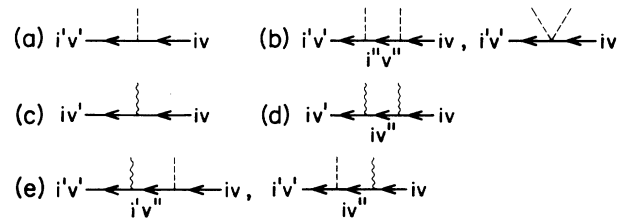


FIG. 1. Transition amplitudes: (a) one-phonon; (b) two-phonon; (c) one-photon; (d) two-photon; (e) one-phonon plus one-photon. Solid lines are molecule propagators while dashed (wavy) lines represent phonons (photons). Intermediate molecule lines in (b), (d), and (e) are dressed.

phonon and photon-assisted contributions. The laser-vibration interaction Hamiltonian H_l (8) in (18) gives the transition rate $L_{ii}^{vv'}$ between internal vibrational states, $v \rightarrow v' = v \pm 1$, due to resonant absorption or emission of a single photon from the laser radiation field. The rate $L_{ii}^{vv'}$ depends linearly on laser intensity I and has a Lorentzian line shape peaked at the vibrational transition frequency (6) with linewidth $\Gamma = \Gamma_v + \Gamma_l$. The laser linewidth Γ_l is typically less than the homogeneous vibrational width Γ_v estimated from infrared absorption data.³⁶ Combining (8) and (18), the vibrational excitation rate is derived^{12,23} to be

$$L_{ii}^{vv'} = \frac{Q^2}{2\epsilon_0\mu c\hbar\Omega} \pi I g(\Omega_l - \Omega + v\Delta) F(\theta) \times [v\delta_{v',v-1} + (v+1)\delta_{v',v+1}] \delta_{i'i} \quad (19)$$

with the line-shape function

$$g(\omega) = \frac{1}{\pi} \frac{\Gamma}{\omega^2 + \Gamma^2} \quad (20)$$

The transition rate depends on the angle of incidence θ of the laser radiation through the function

$$F(\theta) = 4n_r^2 \sin^2\theta \{n_r + [1 + (1 - n_r^{-2})\tan^2\theta]^{1/2}\}^{-2} \quad (21)$$

Here n_r is the index of refraction of the substrate, while Ω_l and c in (19) are the laser frequency and speed of light in vacuum respectively. Note finally that inhomogeneous broadening of the vibrational levels must be treated separately later, and cannot be included in the homogeneous

linewidth Γ in (20).

The first-order phonon-assisted transition rate term is derived from the first derivative term in (13) for the phonon interaction Hamiltonian H_{ph} used in the rate formula (18). The resulting rate $P_{ii}^{vv'}$ describes transitions between bound states in the surface bond, accompanied by the absorption or emission of a single phonon to the solid; one-phonon transitions to all continuum (gas phase) states are denoted by $P_{ci}^{vv'}$. An additional transition rate to the continuum $Q_{ci}^{vv'}$ is induced by the residual Hamiltonian term, H_{res} in (4), which couples molecular translational and internal vibrational motion at the surface. $Q_{ci}^{vv'}$ describes elastic tunneling from excited vibrational levels to excited translational motion. The lowest-order transition rates discussed thus far are described in detail in Ref. 12; their role in stimulating desorption is shown pictorially in Fig. 2.

The calculation of the transition probabilities is now extended to higher orders in perturbation theory to yield additional rate terms due to coherent absorption or emission of two phonons ($D_{ii}^{vv'}$), two photons ($C_{ii}^{vv'}$), and one-phonon-plus-one-photon ($B_{ii}^{vv'}$). The bound-state-bound-state transition matrix is thus

$$R_{ii}^{vv'} = L_{ii}^{vv'} + P_{ii}^{vv'} + B_{ii}^{vv'} + C_{ii}^{vv'} + D_{ii}^{vv'} \quad (22)$$

Note that, in the calculation of these higher-order rates, vibrational anharmonicity is neglected by letting $\Delta = 0$ in (6).

The two-phonon transition rate $D_{ii}^{vv'}$ is obtained by considering transition amplitudes in the rate formula (18) of the form

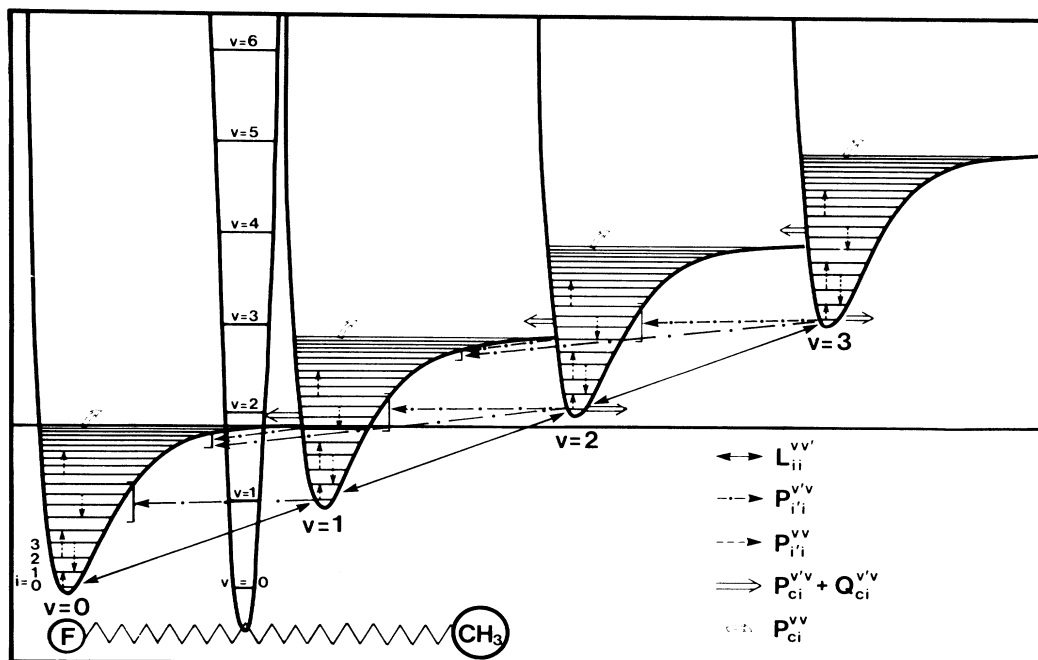


FIG. 2. Energy level diagram for CH₃F on NaCl. Surface potential well corresponding to different vibrational states (v) are transposed laterally for convenience only. Some transition processes included in the theory are indicated by arrows: $P_{ii}^{(v'u)}$ indicates phonon-assisted bound-state-bound-state transitions ($(i,v) \rightarrow (i',v')$); $P_{ci}^{vv'}$ and $Q_{ci}^{vv'}$ are phonon-assisted and elastic tunneling rates from bound states to the continuum; $L_{ii}^{vv'}$ represents the laser coupling.

$$(i\hbar)^{-1} \langle I; p, p'; i', v' | U(\infty) H_{\text{int}}(0) | i, v; \beta, I \rangle \\ = \sum_{j,u} [V(i', v'; j, u; p) G_{ju}^r(\epsilon_j^u + \omega_p) V(j, u; i, v; p') + V(i', v'; j, u; p') G_{ju}^r(\epsilon_j^u + \omega_{p'}) V(j, u; i, v; p)] + V(i', v'; i, v; p, p'). \quad (23)$$

Here, the final state $|p, p'\rangle$ represents the thermal ground state $|\beta\rangle$ plus or minus single-phonon excitations in the modes p and p' , with eigenfrequencies ω_p and $\omega_{p'}$. Molecular states have frequencies ϵ_j^u defined in Appendix A. This transition amplitude contains two kinds of terms, shown in Fig. 1(b). The first terms on the right-hand side of (23), corresponding to the first diagram in Fig. 1(b), arise from taking the first derivative term of the surface potential in (13) to second-order perturbation theory. The one-phonon transition matrix element (or vertex function) $V(i', v'; j, u; p)$ and the intermediate state Green's function $G_{ju}^r(\omega)$ are defined in Appendix A. The final, two-phonon term $V(i', v'; i, v; p, p')$ in the transition amplitude in (23) corresponds to the second diagram in Fig. 1(b) and derives from the second-derivative term in (13) taken to first order in perturbation theory. Additional calculation details are given in Ref. 11.

Squaring the amplitude given above, integrating over all possible bulk Debye phonon final states p and p' , and finally summing over intermediate molecular states, gives the coherent two-phonon-assisted transition rate according to formula (18) as

$$D_{i'v'}^{v'v} = \omega_D A \frac{v_{>}!}{v_{<}!} a^{|v-v'|} (F_1 + F_2 + F_3). \quad (24)$$

Here, ω_D is the Debye frequency of the solid, $v_{>}$ ($v_{<}$) is the greater (lesser) of v and v' , and the coefficients A and a are given by

$$A = 288\pi \frac{\sigma_0^8}{r^6} \frac{m^2}{M_s^2}, \quad \text{and} \quad a = \frac{m_2/m_1}{r\delta_v}. \quad (25)$$

Here, $m = m_1 + m_2$, and the masses m_1 and m_2 , and M_s correspond to either half of the diatomic adsorbed molecule and the unit cell of the solid, respectively, while δ_v is the fundamental vibrational frequency, scaled by ω_D . The dimensionless variables σ_0 and r are related to the Morse surface potential depth V_0 and range γ^{-1} by

$$\sigma_0^2 = \frac{2mV_0}{\hbar^2\gamma^2} \quad \text{and} \quad r = \frac{2m\omega_D}{\hbar\gamma^2}. \quad (26)$$

The transition rate in (24) is composed of three terms F_1 , F_2 , and F_3 . F_1 arises from the second diagram in Fig. 1(b) squared, while F_3 is due to the square of the sum of diagrams of the first type in Fig. 1(b). Cross terms between these two types of diagrams are contained in Fig. 2. Typically, all three of these terms, given below, contribute comparably to the two-phonon transition rate:

$$F_1 = \frac{1}{8} \frac{r^2}{\sigma_0^4} \frac{I(v_{>} - v_M + 1, i', i)}{(|v - v'|!)^2} J_1, \quad (27)$$

$$F_2 = \frac{r}{\sigma_0^2} \frac{I(v_{>} - v_{<} + 1, i', i)}{|v - v'|!} \\ \times \sum_{j=0}^{i_{\max}} \sum_{u=v_{<}}^{v_{>}} \frac{G_{i'v'ju} G_{juv}}{(v_{>} - u)!(u - v_{<}!)} J_2, \quad (28)$$

and

$$F_3 = \sum_{j,j'=0}^{i_{\max}} \sum_{u,u'=v_{<}}^{v_{<}} \frac{G_{i'v'ju} G_{juv} G_{i'v'j'u} G_{j'u'iv}}{(v_{>} - u)!(u - v_{<}!)(v_{>} - u)!(u' - v_{<}!)} J_3. \quad (29)$$

In Eqs. (27)–(29), $I(l, i', i)$ and $F_{i'v'iv}$ are derived from Morse potential matrix elements, while J_1 to J_3 are integrals over the final phonon states, defined in Appendix B. Here, we note only that the integrals J_2 and J_3 involve dressed intermediate molecular states, for which linewidths have been calculated. The restricted sums over intermediate vibrational states (u and u') in F_2 and F_3 are appropriate provided the coefficient a in (25) is much less than unity, as is typically the case.

Computation of the transition rates $D_{i'v'}^{v'v}$ in (24) is accomplished numerically. The coherent two-phonon transition processes appear in the master equation in parallel with the one-phonon transitions given by $P_{i'v'}^{v'v}$, as well as contributing new transitions that are not otherwise possible. While the overall effect of two-phonon transitions on the desorption rates is shown in Sec. III, a general discussion of the rates $D_{i'v'}^{v'v}$ is now in order.

For a deep surface potential in which the lower states i are separated by more than one Debye phonon energy, one-phonon transitions $P_{i\pm 1, i}^{vv}$ are cut off so two-phonon processes $D_{i\pm 1, i}^{vv}$ are essential. At slightly higher states i in the surface potential where one-phonon transitions are possible, the two-phonon term represents only a small correction. However, for the upper, more densely spaced states in the surface potential, the perturbation theory described here breaks down. This occurs when the energy level spacing becomes less than the molecular linewidth. It is clear that transitions involving only the lower, more widely spaced states of translational motion are accurately described by the perturbation theory used here. This fact restricts us to a study of qualitative features of the photo-desorption kinetics in Sec. III.

The coherent absorption or emission of two photons stimulates vibrational transitions $v \rightarrow v' = v \pm 2$ with a rate proportional to laser intensity squared. These transitions parallel incoherent, stepwise, single-photon transition sequences, such as $v \rightarrow v + 1 \rightarrow v + 2$.³⁷ An order-of-magnitude estimate of the size of the coherent two-photon transition rates shows that they are usually much less efficient than the one-photon rate $L^{v'v}$ in stimulating desorption. By considering transition amplitudes of the type shown in Fig. 1(d), the coherent two-photon transition rate $C^{v'v}$ is shown in Ref. 11 to be related to the one-

photon rate $L^{v'v}$ and vibrational linewidth Γ according to

$$C^{20} \approx (L^{10})^2 \Gamma^{-1} . \quad (30)$$

The vibrational linewidths of both intermediate, and initial and final states, have been necessarily incorporated into these estimates.

To compare the efficiency of the two-photon transitions with one-photon processes, an incoherent sequence of one-photon transitions must first be modeled. To do so, we note that one-photon absorption processes occupy the first excited vibrational level with population

$$n_l^1 \approx \frac{L^{10}}{\gamma} n_l^0 , \quad (31)$$

for intensities below saturation. Here γ is the vibrational damping rate due to transitions P_{ii}^{01} and D_{ii}^{01} . Absorption of a second photon with transition rate L^{21} then gives the rate of population of the $v=2$ state as (take $i=0$ for simplicity)

$$L^{21} n^1 \approx \frac{L^{21} L^{10}}{\gamma} n^0 . \quad (32)$$

This is to be compared with the coherent two-photon rate,

$$C^{20} n^0 . \quad (33)$$

The relative importance of coherent versus incoherent processes is obtained by dividing (33) by (32), and using (30) to give

$$\frac{C^{20}}{L^{21} L^{10} \gamma^{-1}} \approx \frac{\gamma}{\Gamma} . \quad (34)$$

For example, for the $\text{CH}_3\text{F}/\text{NaCl}$ adsorption system, we predict $\gamma \approx 10^9 - 10^{10} \text{ s}^{-1}$, compared to $\Gamma = 20 \text{ cm}^{-1}$,³⁶ giving $\gamma/\Gamma \approx 10^{-2}$ to 10^{-3} . Thus, coherent two-photon transitions are insignificant in exciting the $v=2$ level, compared to incoherent sequences of one-photon processes, provided the vibrational damping constant is much smaller than the homogeneous vibrational linewidth. This is just the rapid dephasing limit (where Γ is the dephasing rate), for which Fain and Lin predict that the one-photon rates should dominate.^{8,9} We therefore do not include coherent two-photon transition rates C_{ii}^{vv} in the master equation. However, for some adsorption systems, such as $\text{CO}/\text{Cu}(100)$, for which it is believed²⁵ that $\gamma \approx \Gamma$, coherent processes may be as important as incoherent transitions. In such cases, incoherent processes are still expected to provide a valid qualitative picture of the desorption process.

Finally, we observe that for neither case discussed above are ‘‘high field’’ effects, such as power broadening or Rabi sidebands to be expected.³⁸ The large linewidth of adsorbed molecules makes these features undetectable at all typical laser intensities. The high field regime sets in for $L^{10} \gtrsim \Gamma$, corresponding to laser intensities of the order of $I \sim 10^{10} \text{ W/cm}^2$.

Coherent absorption and emission of one photon and one phonon is described by the transition amplitude

$$(i\hbar)^{-1} \langle k, p; i', v' | U(\infty) H_{\text{int}}(0) | i, \beta, I \rangle$$

$$= \sum_{j,u} [V(i', v'; j, u; k) G_{ju}^r (\epsilon_k^u + \Omega_k) V(j, u; i, v; p) + V(i', v'; j, u; p) G_{ju}^r (\epsilon_j^u + \omega_p) V(j, u; i, v; k)] \quad (35)$$

as shown in Fig. 1(e). Each term above contains a one-photon matrix element $V(i', v'; j, u; k)$ as well as a one-photon vertex $V(j, u; i, v; p)$. Using the amplitude (35) in formula (18), the corresponding transition rate is calculated, in analogy to the two-photon rate described previously. Since the laser line is sharp in comparison with the molecular level widths, the photon spectrum can be assumed to be monochromatic. The coherent one-photon-plus-one-phonon transition rate is then derived to be

$$\begin{aligned} B_{ii}^{v'v} = B_0 \sum_{\delta = \pm \delta_l} & \left[[\Theta(1 - |x|) x n(x)]_{x = (\epsilon_{i'}^{v'} - \epsilon_i^v) / \omega_D + \delta} \right. \\ & \times \sum_{u, u'=0}^{v_{\text{max}}+1} [H_{i'ui'u}^{(1)} P_{i'ui'u}((v'-u)\delta_v + \delta, (v'-u')\delta_v + \delta) + H_{iui'u}^{(2)} P_{iui'u}((v-u)\delta_v - \delta, (v-u')\delta_v - \delta) \\ & \left. + H_{i'ui'u}^{(3)} P_{i'ui'u}((v'-u)\delta_v + \delta, (v-u')\delta_v - \delta)] \right] , \quad (36) \end{aligned}$$

where

$$B_0 = 6\pi\sigma_0^4 r^{-3} m M_s^{-1} \delta_v \delta_l^{-2} F(\theta) Q^2 (\epsilon_0 \mu c \hbar \omega_D^2)^{-2} I \quad (37)$$

and we define

$$\begin{aligned} \delta_l &= \Omega_l / \omega_D , \\ \delta_v &= \Omega_v / \omega_D , \end{aligned} \quad (38)$$

and $F(\theta)$ is given in (21). The Lorentzian-like resonance

functions $P_{iui'u}[x, y]$ are defined in Appendix B. The rate terms $H^{(1)}$ and $H^{(2)}$ are derived from the squares of the first and second terms in the amplitude (25), respectively, while $H^{(3)}$ contains the cross terms. The sums over intermediate surface bound states have been removed in (36) by the one-photon vertex which is diagonal with respect to i states; the sums over intermediate vibrational states, u and u' , are restricted by dipole selection rules contained explicitly in $H_{iui'u}^{(n)}$.

The one-photon-plus-one-photon transition rate, $B_{ii}^{v'v}$,

depends linearly on laser intensity and nonlinearly on temperature through the thermal phonon occupation function $n(x)$ in (36), defined in Appendix A. The rate $B_{i'v}^{iv}$ contributes to transitions where initial and final molecular states are separated by the total energy of one photon and one phonon. Purely vibrational transitions $v \rightarrow v + 1$ are slightly enhanced by one-photon-plus-one-phonon processes, and new transitions such as $(i,v) = (0,0) \rightarrow (1,1)$ may be accessed directly. While the intensity dependence of the desorption rate is not altered qualitatively (in a log-log graph) by the inclusion of coherent one-photon-plus-one-phonon transitions, the photodesorption yield line shape may be affected in an asymmetric manner, as shown in the next section.

C. Inhomogeneous vibrational spectrum

The discussion has thus far dealt exclusively with desorption from a homogeneous adsorbate. To include inhomogeneous line broadening¹⁴ as well, we now assume that the vibrational frequencies of the adsorbed molecules are statistically distributed around some mean frequency $\bar{\Omega}$. Denoting by $f(\Omega - \bar{\Omega})d\Omega$ the probability of having a molecule with vibrational frequency in the interval $d\Omega$ around Ω , the total coverage is then proportional to

$$\int d\Omega f(\Omega - \bar{\Omega}) \sum_{i,v} n_{i,v}^i(\Omega; t), \quad (39)$$

where $n_{i,v}^i(\Omega; t)$ is the probability for a molecule with vibrational frequency Ω to be found in the state iv . Differentiating with respect to time gives the mean desorption rate per adsorbed molecule, in analogy with (2),

$$R_d^{\text{ih}}(\bar{\Omega}, \Omega_l; I) = \int_0^\infty d\Omega r_d(\Omega, \Omega_l; I) f(\Omega - \bar{\Omega}) \quad (40)$$

after the initial transients have died away. Here, $r_d \propto \lambda_0$ —the smallest eigenvalue of the rate matrix—is a function of laser frequency Ω_l which is peaked at Ω with spectral width related to the homogeneous vibrational width Γ . In the absence of heterogeneity, $f(\Omega - \bar{\Omega})$ become sharp and the desorption rate in (40) is equal to the homogeneous rate constant $r_d(\bar{\Omega}, \Omega_l; I)$. In practice, we chose the statistical distribution function $f(\Omega - \bar{\Omega})$ to be a Gaussian with width Γ_s .

To see the effects of inhomogeneity on the desorption rate constant, it is useful to consider the limit $\Gamma_s \gg \Gamma$, corresponding to a predominantly inhomogeneously broadened infrared absorption spectrum. In this limit, the laser excites effectively only those molecules with vibrational frequency Ω resonant with the photon frequency Ω_l , and Eq. (40) reduces to

$$R_d^{\text{ih}}(\bar{\Omega}, \Omega_l; I) \cong f(\Omega_l - \bar{\Omega}) \int_0^\infty d\Omega r_d(\Omega, \Omega_l; I), \quad \Gamma_s \gg \Gamma. \quad (41)$$

In most, but not all cases, the integral above is a slowly varying function of Ω_l , and the spectral line shape of the net desorption rate R_d^{ih} is then identical with the infrared absorption spectrum given by $f(\Omega_l - \bar{\Omega})$. Comparing the on-resonant desorption rates R_d^{ih} and r_d in the presence and absence, respectively, of inhomogeneity, (41) gives the order-of-magnitude estimate

$$\frac{R_d^{\text{ih}}(\bar{\Omega}, \Omega_l = \bar{\Omega}; I)}{r_d(\bar{\Omega}, \Omega_l = \bar{\Omega}; I)} \approx \frac{\Gamma}{\Gamma_s} \quad \text{for } \Gamma_s \gg \Gamma. \quad (42)$$

Thus, only the fraction Γ/Γ_s of the adsorbate population can effectively participate in resonant photodesorption. In the next section, we will show that, for some adsorption systems, additional structure may be realized in the photodesorption yield line shape.

III. RESULTS

The photodesorption rate constant is now calculated for typical experimental situations, by solving the master equation incorporating the microscopic transition rates described above. The dependence of the desorption rate on both laser intensity and on laser frequency are predicted so that a qualitative comparison with experimental results in the literature can be made. We recall that the desorption rate constant is proportional to the yield per laser pulse, according to Eq. (3).

A. Desorption rate versus laser intensity

Photodesorption of CH_3F physisorbed on $\text{NaCl}(102)$ will be considered first in detail,²⁻⁴ before results for other adsorption systems—pyridine on KCl , CO on Cu , and CO on NaCl —are presented. By studying the intensity dependence of the desorption rate constant r_d , with the laser tuned on resonance, $\Omega_l = \Omega$, the influence of the heat of adsorption and of microscopic two-quantum transitions is observed. For simplification, we assume at first that the internal molecular vibration mode is harmonic, that is $\Delta = 0$ in (6).

To model the adsorption of CH_3F on NaCl , we assume that a CH_3F molecule physisorbs in a (Morse) potential well with depth V_0 equal to the heat of adsorption. It is oriented with the F atom closest to the surface and the C-F axis perpendicular to the surface. The relevant vibrational mode is the ν_3 vibration of CH_3 against F; these are then the two masses in our “diatomic” approximation. The experimentally measured heat of adsorption³ varies from $V_0 = 22.5$ to 46 kJ/mole, for coverages from multilayer to monolayer, respectively.²⁻⁴ The range γ^{-1} of the surface potential is unknown, so we assume a typical value $\gamma^{-1} = 0.37 \text{ \AA}$ for our calculations. The laser, incident at an angle of 60° to the surface normal, is tuned on resonance with the frequency $\Omega = 970 \text{ cm}^{-1}$ of the internal ν_3 vibrational mode, which has a linewidth $\Gamma \approx 24 \text{ cm}^{-1}$.³⁶ We assume for now that the experimental infrared absorption linewidth is purely homogeneously broadened, and later estimate the changes to be made if the inhomogeneity is significant. The infrared absorption intensity is characterized by the dynamic dipole moment μ_{dyn} , or effective charge Q in our case, which are related by

$$Q = \mu_{\text{dyn}} \sqrt{2\mu\Omega/\hbar} \approx 1 \text{ electronic charge}. \quad (43)$$

(μ on the right-hand side is the molecular reduced mass.)

In Fig. 3, the desorption rate constant r_d is graphed versus laser intensity for the $\text{CH}_3\text{F}/\text{NaCl}$ system for the three heats of adsorption $V_0 = 22.5, 33,$ and 46 kJ/mole

at the temperature $T=100$ K. Note that, for the latter two values, coherent two-phonon transitions are essential to couple the lower surface bound states. It is seen that the desorption rate increases nonlinearly with laser intensity, and saturates at very high intensity.

For $V_0=22.5$ kJ/mole, the desorption rate previously predicted by the single-photon-single-phonon theory¹² is included as the dashed line. A comparison with the full two-quantum graph shows that the inclusion of coherent higher-order transition processes shifts the desorption rate constant to higher laser intensities. This shift is due to efficient two phonon rates which reinforce single-phonon transitions within the surface well via $D_{i'v}^{v'v}$ and significantly increase vibrational damping due to coupling between vibrational and surface bound states by, for example, aiding transitions such as $(i=0, v=1)$ to $(i=5, v=0)$. Consequently, saturation occurs at higher intensities and with higher desorption rates. However, these vibrational damping rates are not accurately determined by perturbation theory due to the strength of the phonon coupling in this system, as discussed in Sec. II. This fact, combined with the experimental uncertainty in determining the ir absorption intensity per adsorbed molecule, makes absolute calibration of the intensity axis in Fig. 3 imprecise.

With this in mind, we can compare our results with experimental measurements of Heidberg *et al.*³ that give $r_d \approx 2 \times 10^5$ s⁻¹ at $I = 3 \times 10^5$ W/cm², increasing with intensity $r_d \propto I^{2.8}$ in the multilayer coverage case. These data fall at slightly lower intensity than the dashed line in Fig. 3, and the intensity dependence is steeper, more in line with the $V_0=33$ kJ/mole graph. Owing to uncertainties noted previously, a conclusive comparison between theory and experiment cannot yet be made.

Nevertheless, it is apparent in Fig. 3 that, as the heat of adsorption V_0 is increased, the desorption rate is shifted to higher intensities and becomes increasingly nonlinear in intensity. At moderate intensity and at fixed temperature,

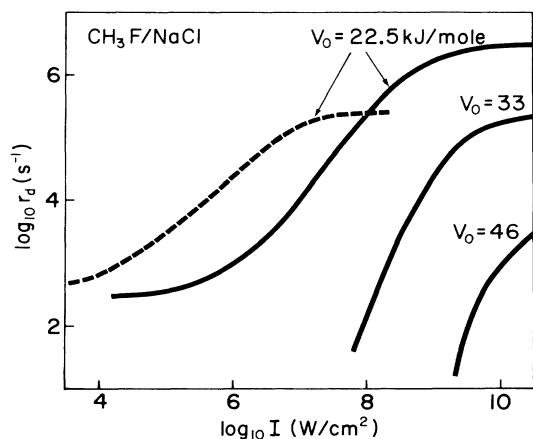


FIG. 3. Photodesorption rate versus laser intensity for $\text{CH}_3\text{F}/\text{NaCl}$ for different adsorption energies V_0 . Dashed line is without coherent two-quantum processes. $T=100$ K; $\Gamma=24$ cm⁻¹; $\gamma^{-1}=0.37$ Å; $\Delta=0$.

the graphs may be parametrized in the harmonic case ($\Delta=0$) by the power-law dependence

$$r_d(\Omega, \Omega_l; I) \propto [g(\Omega_l - \Omega)I]^\alpha. \quad (44)$$

Note that the vibrational line-shape function g , given in (20), and the laser intensity I enter the vibrational excitation rate $L^{v'v}$, and hence r_d , together. The exponent α is generally less than the level of vibrational excitation v^* required to bring a molecule in the translational ground state ($i=0$) into degeneracy with the continuum of gas-phase states. The maximum slopes of the three solid curves in Fig. 3 give exponents $\alpha=1.4, 2.6,$ and 3.7 , for heats of adsorption $V_0=22.5, 33,$ and 46 kJ/mole, respectively. These exponents are slightly less than the corresponding values of $v^*=2, 3,$ and 4 . These differences indicate that thermal (phonon-assisted) population of excited i states with $v < v^*$, from which desorption is already possible, can in fact play a role in the photodesorption process.

Thus far, we have attributed the experimentally observed (ir) vibrational linewidth, $\Gamma_{\text{ir}}=\Gamma+\Gamma_s$, to homogeneous broadening processes, and thus let

$$\Gamma_{\text{ir}}=\Gamma, \quad \Gamma_s=0 \quad (45)$$

in the calculation of r_d . To see the maximum possible effect of inhomogeneous linewidth contributions Γ_s in photodesorption, we now suppose

$$\Gamma_{\text{ir}}=\Gamma_s \gg \Gamma \quad (46)$$

to calculate R_D^{ih} . Using Eq. (39) to include the true homogeneous linewidth contribution Γ and inhomogeneous part Γ_s correctly, we derive the estimate

$$\frac{r_d}{R_D^{\text{ih}}} = O((\Gamma/\Gamma_{\text{ir}})^{\alpha-1}) \quad \text{if } \Gamma \ll \Gamma_{\text{ir}}, \quad (47)$$

where α is the exponent in Eq. (44). The desorption rate constants shown in Fig. 3 may thus be underestimated by at most the factor given above. Although the relative contributions of homogeneous and heterogeneous effects in Γ and Γ_s , respectively in the total vibrational linewidth are presently unknown, inclusion of inhomogeneous line broadening makes the agreement between the theoretical results of Fig. 3 and experiment closer. Note that, only if the photodesorption yield depends linearly on the laser intensity ($\alpha=1$), does the convolution formula (38) reduce roughly to adding Γ_s directly to Γ in the laser rate $L^{v'v}$, making the distinction between homogeneous and heterogeneous effects less important in that case.

Resonant photodesorption has also been observed experimentally from the adsorption systems pyridine/ KCl ⁵ and CO/NaCl .⁴ These systems are now modeled theoretically, including coherent two-phonon transition processes $D_{i'v}^{v'v}$ and vibrational anharmonicity Δ in $L^{v'v}$ (19). Rather than solving the master equation (1) by direct numerical inversion, an analytic diagram method due to Hill^{39,40} is used to deduce a simplified (approximate) recursion formula for the quasistationary occupation functions n_i^v and hence the desorption rate constant.¹¹ The latter method is advantageous for more

strongly bound adsorption systems because the complexity of the numerical computation is vastly reduced, and accurate calculation of extremely slow desorption rates is possible.

The desorption kinetics calculated in this way for the pyridine/KCl system are shown in Fig. 4. While our theory is more suitable for a diatomic molecule than for pyridine, qualitative predictions can still be made. Lacking knowledge of the exact molecular orientation and of the vibrational dipole moment, the intensity axis can only be approximately calibrated. With heat of adsorption $V_0 \approx 3900$ K and vibrational frequency $\Omega = 1032$ cm^{-1} , excitation to the third vibrational level $v^* = 3$ is important. Solid lines in Fig. 4 give the dependence of desorption rate on laser intensity in: (i) the harmonic approximation $\Delta = 0$ and (ii) with an anharmonic shift $\Delta = 25$ cm^{-1} included. Since $v^* > 1$, increased anharmonicity leads to considerably decreased desorption rates. However, lateral vibrational energy transfer may counteract this effect somewhat, as is shown elsewhere.¹⁸ At a laser intensity $I = 1$ MW/cm^2 , the $\Delta = 0$ graph has a slope of 1.7, in close agreement with the nonlinear intensity dependence $r_d \propto I^{1.8}$, observed by Chuang at this intensity.⁵ However, it must be cautioned that the analogous desorption rate calculation based on only single-phonon transitions is shifted to considerably higher intensities, as shown by the dashed line in Fig. 4. This clearly shows once again the importance of coherent multiphonon transitions in the photodesorption process; this fact restricts us to a qualitative discussion of the kinetics.

Strongly nonlinear desorption behavior is also predicted for CO from Cu(100), for which the heat of adsorption and vibrational frequency are roughly double that for py-

ridine on KCl. With system parameters for CO in the on-top site, $V_0 = 8350$ K, $\gamma^{-1} = 0.34$ Å, $\Omega = 2010$ cm^{-1} , $Q = 0.5e$, and $\Gamma = 5$ cm^{-1} , we predict that

$$r_d \approx (I[\text{MW}/\text{cm}^2])^3 \text{ s}^{-1} \text{ for } \Delta = 0 \text{ and } I \lesssim 10. \quad (48)$$

Including a vibrational anharmonic shift of $\Delta = 25$ cm^{-1} reduces r_d by an order of magnitude.

The theoretical path to desorption is essentially the same for both the CO/Cu(100) and pyridine/KCl(100) systems. Photoinduced vibrational excitation to the $v = 3$ level is followed by phonon-assisted tunneling between bound states, i.e., $(i = 0, v = 3) \rightarrow (i, v = 2) \rightarrow (j', v = 1) \rightarrow (i'', v = 0)$ where $0 < i < i' < i''$. This process uses up vibrational energy to excite successively higher levels of translational motion in the surface bond. In fact, desorption occurs here from the very top states (i'') of the surface potential, which have population levels that are many orders of magnitude greater than their thermal equilibrium occupations.

Finally, we present calculations of the photodesorption kinetics of ^{13}CO from NaCl. For this weakly bound adsorption system the internal C-H vibrational frequency is larger than the adsorption energy, so population of the first excited vibrational level is sufficient to stimulate photodesorption by tunneling to the gas phase. However, vibrational relaxation by coupling to bound surface states of frustrated translational motion is cut off because of the large energy difference. In this situation, the one dimensional, single ad molecule model used here cannot describe the dominant vibrational damping channel. An additional, phenomenological damping constant γ has been included in the calculations to represent vibrational coupling to librational and/or bending modes and to collective motion involving other adsorbed molecules. In Fig. 5, the desorption kinetics are shown for three possible values of the vibrational damping constant. In each case, the desorption rate increases linearly with laser intensity.

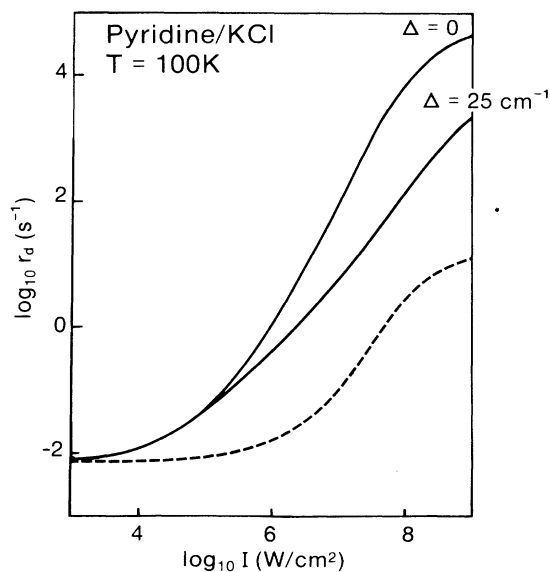


FIG. 4. Desorption rate versus laser intensity for pyridine on KCl, for different choices of vibrational anharmonicity Δ . The broken line is obtained by omitting coherent two-phonon transition processes. System parameters are $V_0 = 3900$ K; $\gamma^{-1} = 0.3$ Å; $\Gamma = 10$ cm^{-1} ; $Q = 1$ electronic charge.

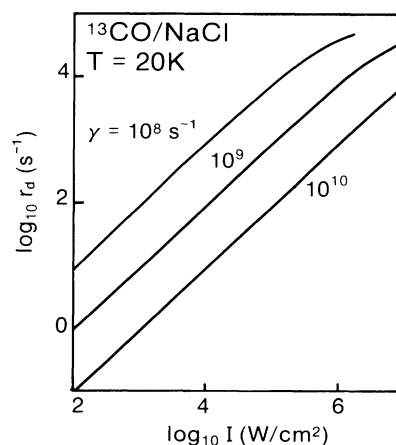


FIG. 5. Desorption rate vs laser intensity for CO on NaCl, for different vibrational damping rates γ . System parameters are $V_0 = 1960$ K; $\gamma^{-1} = 0.3$ Å; $\Omega = 2160$ cm^{-1} ; $\Gamma = 14$ cm^{-1} ; and $Q = 1e$.

B. Line shape of the photodesorption rate constant

Since photodesorption is initiated by resonant vibrational excitation, the resulting desorption yield must also exhibit a resonant spectral line shape. The dependence of the photodesorption rate constant on laser frequency can differ from the corresponding infrared absorption spectrum due to nonlinear and coherent processes, vibrational anharmonicity, and surface heterogeneity, as described individually below.

In the absence of vibrational anharmonicity and inhomogeneity, the nonlinear intensity dependence of desorption, discussed above, was parametrized by Eq. (44). While the desorption rate thus depends on the α th power of the laser intensity, the photodesorption spectrum is given by the α th power of the vibrational line shape or infrared spectrum as discussed previously by Wu *et al.*⁹ For $\alpha > 1$, the desorption yield line shape is narrower than the infrared absorption line, while for $\alpha < 1$, the reverse is true. The desorption yield line width (FWHM) is given, according to (20) and (44), by $(2^{1/\alpha} - 1)^{1/2}$ times the infrared absorption linewidth Γ .⁹ Only in the linear case $\alpha = 1$, as seen in Fig. 5 for CO on NaCl, are the photodesorption and infrared absorption linewidths equal. At the intermediate laser intensities used experimentally, it is found in Figs. 3 and 4 that $\alpha > 1$ and thus line narrowing is predicted for the CH₃F/NaCl and pyridine/KCl systems. For example, the theoretical desorption rate follows $r_d \propto I^{1.9}$ for CH₃F on NaCl at $T = 65$ K and $I = 1$ MW/cm². The photodesorption line shape at this intensity is shown in Fig. 6 to be narrower than the infrared absorption line by a factor of ≈ 0.7 . However, the inclusion of the vibrational anharmonicity will be shown later to partially cancel this narrowing effect.

At high intensities, the slopes of the r_d versus I curves in Fig. 3 decrease eventually to zero as saturation sets in

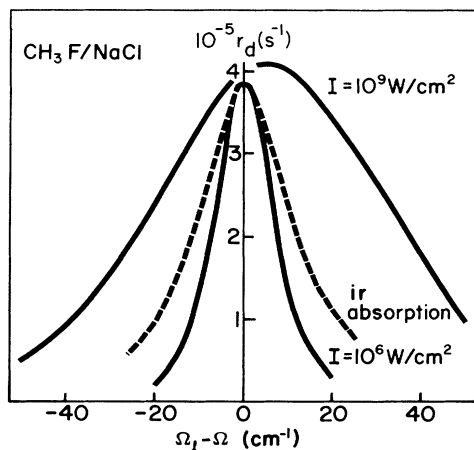


FIG. 6. Photodesorption line shape calculated with coherent two-quantum processes included in harmonic case $\Delta = 0$. Dashed line represents ir absorption spectrum, while solid lines are desorption rates at intensities $I = 1$ and 10^3 Mw/cm² and $T = 65$ K for CH₃F/NaCl with the same model parameters as in Fig. 3.

and the photodesorption line shape broadens, as shown in Fig. 6. At $I = 10^3$ MW/cm², the spectral width of the photodesorption rate increases to 60 cm⁻¹ because detuning the laser frequency does not reduce the desorption yield appreciably until the photon (and one-photon-plus-one-phonon) transition rates are reduced below the saturation level. Thus, the tails of these transition rates affect the desorption spectrum markedly at saturation. The spectra show asymmetry due to one-photon-plus-one-phonon transitions which favor (spontaneous) phonon emission ($\Omega_l - \Omega > 0$) over (thermal) phonon absorption ($\Omega_l - \Omega < 0$) at low temperatures. Since the asymmetry of the one-photon-plus-one-photon rate occurs on the frequency scale with which the phonon thermal occupation function varies, i.e., $\Delta v = k_B T / h \approx 45$ cm⁻¹ at $T = 65$ K, asymmetric desorption yields may be expected when the spectral width is of the order of T .

In addition, the tails of the infrared absorption spectrum itself become asymmetric at large detunings because the frequency dependence of the vibrational linewidth and line shift must then be taken into account. This second effect, although not taken into account in Fig. 6, is anticipated to contribute to the asymmetry of the desorption line shape in a manner similar to that of the one-photon-plus-one-phonon rates considered above.

The influence of vibrational anharmonicity on the photodesorption spectrum is now addressed. Since the anharmonic energy defect Δ is of roughly the same order as the vibrational linewidth Γ of adsorbed molecules, anharmonic effects may be expected to appear in the photodesorption line shape. For an adsorption system such as CH₃F on NaCl, excitation of both the $v = 0 \rightarrow 1$ and $v = 1 \rightarrow 2$ transitions is necessary to induce desorption. A laser tuned to the lowest-energy spacing, i.e., $\Omega_l = \Omega$, will be slightly off resonance with respect to higher transitions. Photodesorption may be most efficient at some intermediate frequency. In this way the desorption kinetics may serve as a probe of higher vibrational energy levels.

The desorption line shape is now predicted by solving the master equation (1) with coherent two-quantum transitions neglected. The vibrational anharmonicity Δ makes its main contribution in the photon absorption rate $L^{v'v}$ in equation (19). The minor effect of Δ on phonon-assisted transitions $P_{i'v'}^{v'v}$ is neglected.²³ In Fig. 7, the photodesorption spectrum is plotted for the CH₃F/NaCl for laser intensity $I = 1$ MW/cm² at $T = 50$ K. The vibrational linewidth³⁶ $\Gamma = 20$ cm⁻¹ is only slightly larger than the anharmonic shift $\Delta = 16$ cm⁻¹ obtained from gas-phase and matrix isolation measurements.^{41,42} The desorption spectrum is shifted to the red of the harmonic case, and is also broadened as the anharmonicity is increased. These features result from the dependence of the desorption rate on the vibrational excitation rates of both the $v = 0 \rightarrow 1$ and $v = 1 \rightarrow 2$ transitions. The product of the line shapes of these two transitions, $g(\Omega)g(\Omega - \Delta)$, is found to agree well with the desorption spectrum. This is in agreement with the calculated intensity dependence, $r_d \propto I^{1.9}$ for the conditions in Fig. 7, showing that the $v = 0 \rightarrow 1$ and $v = 1 \rightarrow 2$ transitions contribute nearly equally to desorption.

For comparison, we now examine a model adsorption

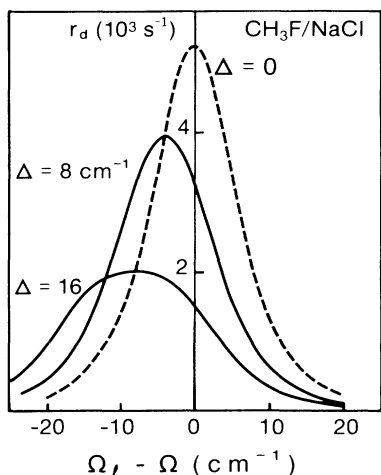


FIG. 7. Photodesorption line shape for $\text{CH}_3\text{F}/\text{NaCl}$. Solid lines are vibrational anharmonicity $\Delta=8$ and 16 cm^{-1} ; harmonic case $\Delta=0$ is given as dashed line. Also $\Gamma=20\text{ cm}^{-1}$ and laser intensity is $I=1\text{ MW/cm}^2$. Surface potential parameters are $V_0=22.5\text{ kJ/mole}$ and $\gamma^{-1}=0.3\text{ \AA}$.

system in which the anharmonic defect is larger than the vibrational linewidth. Infrared absorption measurements for CO adsorbed on $\text{NaCl}(100)$ give $\Delta=24\text{ cm}^{-1}$ and $\Gamma=14\text{ cm}^{-1}$.²² However, the $v=1\rightarrow 2$ transition is not expected to contribute significantly to desorption for this system, since the adsorption well depth $V_0=2177\text{ K}$ is less than the vibrational energy $\hbar\Omega=3100\text{ K}$, permitting desorption directly from the $v=1$ level. To study the $\Delta > \Gamma$ case, we therefore modify the $\text{CH}_3\text{F}/\text{NaCl}$ system by choosing $\Delta=20\text{ cm}^{-1}$ and $\Gamma=10\text{ cm}^{-1}$. The desorption spectrum for this hypothetical system is shown in Fig. 8 to be double peaked. The desorption rate is max-

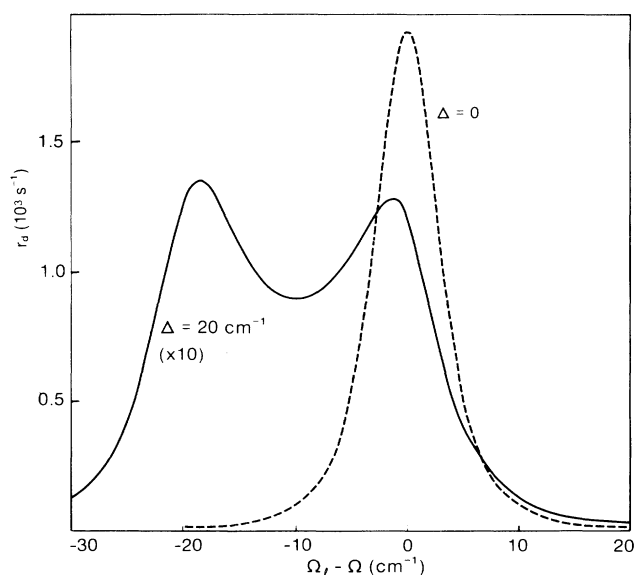


FIG. 8. Photodesorption line shape for a modified $\text{CH}_3\text{F}/\text{NaCl}$ system. Vibrational mode parameters are $\Gamma=10\text{ cm}^{-1}$; $\Delta=20\text{ cm}^{-1}$ (solid line); other parameters as for Fig. 7.

imized by tuning the laser near either the $v=0\rightarrow 1$ or $v=1\rightarrow 2$ transition frequency. The peaks are of roughly equal height because both transitions contribute equally to the desorption process. This spectrum is in sharp contrast to the infrared absorption line shape which sees only the $v=0\rightarrow 1$ transition.

The influence of inhomogeneous broadening of the vibrational line shape of the photodesorption spectrum is now studied. (We ignore coherent two-quantum transition processes and vibrational anharmonicity for simplicity here.) In Sec. II C, it was shown that, when the inhomogeneous contribution Γ_s to the vibrational linewidth is much larger than the homogeneous part Γ , the photodesorption yield spectrum will usually coincide with the Gaussian infrared absorption line shape. This analysis was based on Eq. (39), for which the right-hand term

$$\int_0^\infty d\Omega r_d(\Omega, \Omega_l; I) \quad (49)$$

was assumed to vary slowly as a function of the vibrational frequency Ω . This is in fact the case for the $\text{CH}_3\text{F}/\text{NaCl}$ adsorption system with potential parameters $V_0=22.14\text{ kJ/mole}$ and $\gamma^{-1}=0.36\text{ \AA}$.

However, additional structure in the inhomogeneous photodesorption line shape is also possible. By adjusting the surface potential parameters slightly to give $V_0=23.05\text{ kJ/mole}$ and $\gamma^{-1}=0.364\text{ \AA}$, a double-peaked desorption spectrum dramatically appears in Fig. 9. Although this small increase in V_0 is below experimental accuracy, the theoretical appearance of a double-peaked photodesorption line shape is easily explained. Desorption occurs predominantly from the $i=6, v=1$ state at the temperature and intensity given, via transition rates $Q_{c6}^{01} + P_{c6}^{01}$. The elastic tunneling rate, Q_{c6}^{01} , is cut off when

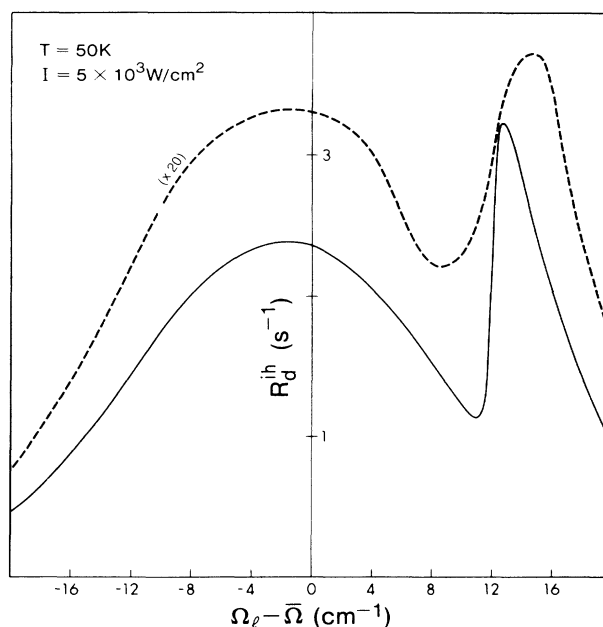


FIG. 9. Photodesorption line shape as for Fig. 8, but with slightly deeper surface potential $V_0=23.05\text{ kJ/mole}$ and $\gamma^{-1}=0.364\text{ \AA}$. Solid and dashed lines are for $\Gamma=1\text{ cm}^{-1}$ and $\Gamma=10\text{ cm}^{-1}$, respectively.

$\epsilon_6 < 0$, which corresponds to $\bar{\Omega} < \Omega + 12 \text{ cm}^{-1}$. At lower laser frequencies Ω_l , the molecules with lower vibrational frequency $\Omega \approx \Omega_l$ desorb preferentially in (39), via the rate P_{c6}^{01} and other transitions. However, for $\Omega_l > \bar{\Omega} + 12 \text{ cm}^{-1}$, the laser selectively excites molecules with $\Omega \approx \Omega_l$ for which the additional tunneling transition Q_{c6}^{01} is operative. As a result, the overall desorption rate is suddenly enhanced, leading to a double-peaked spectrum. The infrared absorption line shape, on the other hand, is simply given by the Gaussian vibrational-frequency distribution $f(\bar{\Omega} - \Omega_l)$.

The dashed line in Fig. 9 shows that the double peak is only slightly rounded out by homogeneous vibrational line broadening. Note that the widths of the surface bond energy levels E_j , which have not been included here, will also tend to smooth out the structure in Fig. 9.

In summary, we find that the line shape of the photo-desorption yield need not coincide with the corresponding infrared vibrational mode of the adsorbed molecule. The incoherent multiphoton excitation processes that cause the nonlinear intensity dependence of desorption yields [i.e., $\alpha > 1$ in (44)] also lead to either a narrower desorption spectrum for $\Delta \ll \Gamma$, a red shifted and slightly broader line shape for $\Delta \lesssim \Gamma$, or a multiple-peaked spectrum for $\Delta \gtrsim \Gamma$. These results are valid in the low-coverage limit.

Experimental line shapes for both the photodesorption yield and infrared absorption have been measured by Heidberg *et al.* for the $\text{CH}_3\text{F}/\text{NaCl}$ (Refs. 3 and 36) and CO/NaCl (Refs. 4 and 22) systems. For the latter system, the observed line shapes for infrared absorption and for desorption have the same width, as predicted by the theory, since $\nu = \alpha = 1$. For the $\text{CH}_3\text{F}/\text{NaCl}$ system, on the other hand, the infrared absorption spectrum at multi-layer coverage receives contributions from molecules at three distinct adsorption sites, whereas photodesorption must occur predominantly from the most weakly bound adsorbed species (see Fig. 3). As a result of this complication, experimental confirmation of the specific theoretical line shape shown in Fig. 7 is not yet possible, although the results are consistent within the uncertainties present.

IV. CONCLUSIONS

This paper has described a theory of resonant photo-desorption at low coverage, mediated by tunneling of vibrational energy into the frustrated translational mode of an adsorbed molecule. Anharmonicity and inhomogeneous broadening for the internal vibrational mode, as well as coherent two-quantum transition processes, have been included to more realistically model experimental systems. The desorption rate constant depends on laser intensity through the nonlinear power law $r_d \propto I^\alpha$, in general agreement with experimental results. The degree of nonlinearity depends on both the energetics of the system, i.e., the ratio of adsorption energy to the vibrational frequency, and on the efficiency of intramolecular coupling that pumps the molecular translational mode. The line shape of the photodesorption yield may differ from the corresponding infrared absorption spectrum due to the combined effects of nonlinearity, vibrational anharmonicity, and surface heterogeneity.

While the theory presented here is strictly valid in only the low-coverage limit $\Theta \ll 1$, experiments are typically performed at monolayer to multilayer coverages. To describe photodesorption at these higher coverages, the additional mechanisms of lateral V - V energy transfer and of resonant surface heating have been discussed elsewhere.¹⁵⁻¹⁸ Since these processes can stimulate desorption after laser pumping of only the first excited vibrational level, the dependence of the desorption yield on vibrational anharmonicity is reduced. On the other hand, a nonlinear intensity dependence remains. To the extent that the low-coverage predictions given here are relevant to typical experimental situations, we predict that photodesorption of CO from Cu(100) may be expected to occur with about the same efficiency as that of pyridine on KCl, at a laser intensity of $1 \text{ MW}/\text{cm}^2$.

To better quantify the theoretical predictions, it is necessary to accurately characterize the adsorption system experimentally. The depth and range of the surface potential and the infrared absorption intensity must be determined for known coverage. Of these, only the heat of adsorption is known for the photodesorption systems studied experimentally thus far. In addition, a direct check of the calculated vibrational damping rates, by picosecond relaxation techniques⁴³ for example, would be useful. The importance of the photodesorption mechanism discussed here could then be better established.

ACKNOWLEDGMENTS

The generous hospitality of Professor J. H. Block, Fritz-Haber-Institut, Berlin, during the writing of this manuscript, is sincerely appreciated. This work was supported in parts by grants from the Natural Science and Engineering Research Council of Canada.

APPENDIX A

The vertex functions describing one-photon, one-phonon, and two-phonon emission are given, respectively, by

$$V(i', v'; i, v; k) = -\frac{Q}{\mu} \left[\frac{\hbar}{2\epsilon_0} \right]^{1/2} \times \left\langle i', v' \left| \frac{\partial}{\partial \xi} V \left[x - \frac{\mu}{\mu_1} \xi \right] \right| i, v \right\rangle \times \Omega_k^{-1/2} \mathbf{n} \cdot \mathbf{U}_k(0) (1 + n_k)^{1/2}, \quad (\text{A1})$$

$$V(i', v'; i, v; p) = -\frac{1}{i\hbar} \left\langle i', v' \left| \frac{\partial}{\partial \xi} V \left[x - \frac{\mu}{\mu_1} \xi \right] \right| i, v \right\rangle \times \left[\frac{\hbar}{2M_s N_s} \right]^{1/2} \frac{\hat{\mathbf{e}}_p \cdot \mathbf{n}}{\omega_p^{1/2}} (1 + n_p)^{1/2}, \quad (\text{A2})$$

and

$$\begin{aligned}
V(i', v'; i, v; p, p') &= \frac{1}{2i\hbar} \left\langle i', v' \left| \frac{\partial^2}{\partial x^2} V \left[x - \frac{\mu}{\mu_1} \xi \right] \right| i, v \right\rangle \\
&\times \frac{\hbar}{2m_s n_s} \frac{(\hat{\mathbf{e}}_p \cdot \mathbf{n})(\hat{\mathbf{e}}_{p'} \cdot \mathbf{n})}{\omega_p^{1/2} \omega_{p'}^{1/2}} \\
&\times (1+n_p)^{1/2} (1+n_{p'})^{1/2}. \quad (\text{A3})
\end{aligned}$$

Here, n_k and n_p are the occupation functions of the photon and phonon fields, respectively. Phonon- and photon-absorption processes are obtained by replacing the corresponding $(1+n)^{1/2}$ factor with $n^{1/2}$ in the above. (Note that the relevant photon occupation function is large when the laser is tuned to the vibrational resonance so we approximate $n_k + 1 \approx n_k$ in the laser-assisted transition rates.)

The phonon occupation function is given by

$$n(x) = n_p = [\exp(\hbar\omega_p/k_B T) - 1]^{-1} \quad (\text{A4})$$

with the dimensionless phonon frequency x , defined by $\omega_p = x\omega_D$, used in (36).

The molecular state Green's functions are given by

$$G_{iv}^r(\omega) = \frac{1}{\omega - \varepsilon_i^v - i\Sigma_{iv}(\omega)}, \quad (\text{A5})$$

where the molecular eigenfrequency is

$$\begin{aligned}
\varepsilon_i^v &= -\frac{\omega_D}{r} (\sigma_0 - i - \frac{1}{2})^2 + v\Omega, \\
i &= 0, 1, \dots, i_{\max}, \quad v = 0, 1, \dots.
\end{aligned} \quad (\text{A6})$$

The self-energy correction $i\Sigma_{iv}(\omega)$ is calculated in perturbation theory, including the diagrams shown in Fig. 10 below. The first two terms give only pure imaginary contributions to Σ_{iv} , and are ignored since we need only include the real, linewidth contributions in (A5).

The real parts of the last three terms in Fig. 10 are evaluated¹¹ to give

$$\text{Re}\Sigma_{iv}(\varepsilon_i^v) = -\frac{1}{2} \left[\sum_{i'=0}^{i_{\max}} \sum_{v'=0}^{v_{\max}} [P_{ii'}^{v'v} + D_{ii'}^{v'v}(1)] + \sum_{v'=0}^{v_{\max}+1} L^{v'v} \right] \quad (\text{A7})$$

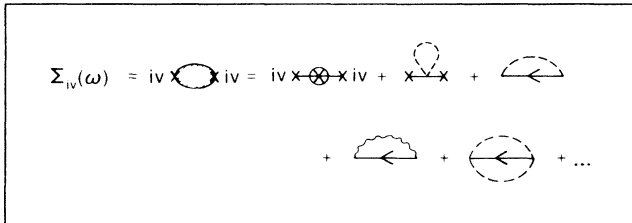


FIG. 10. The molecular self-energy. Solid, dashed, and wavy lines represent molecule, phonons, and photons, respectively.

representing the net transition rate out of the state iv . Transitions to the continuum, $P_{ci}^{v'v}$ and $Q_{ci}^{v'v}$, are too slow to contribute significantly to the linewidth and have been ignored here. The laser-assisted rates $L^{v'v}$ are also negligible in (A6) at intensities below saturation. $D_{ii}^{v'v}(1)$ represents the F_1 term in (24). The sum over $i'v'$ in (A7) includes the diagonal terms P_{ii}^{vv} and $D_{ii}^{vv}(1)$ which describe dephasing processes due to soft phonon absorption and elastic phonon scattering, respectively, and are given in Ref. 11.

APPENDIX B

The functions I and G appearing in Eqs. (27)–(29) are given by

$$G_{i'v'iv} = \begin{cases} I(|v-v'|, i', i) & (i', v') \neq (i, v) \\ \frac{a}{2} (2v+1) I(2, i, i) & (i', v') = (i, v) \end{cases} \quad (\text{B1})$$

and

$$\begin{aligned}
I(l, i, i') &= \frac{1}{\sigma_0} \left[\frac{i_{>}! \Gamma(2\sigma_0 - i_{>})}{i_{<}! \Gamma(2\sigma_0 - i_{<})} (\sigma_0 - i - \frac{1}{2})(\sigma_0 - i' - \frac{1}{2}) \right]^{1/2} \\
&\times \left[2^l \frac{|i-i'|}{2\sigma_0} (2\sigma_0 - i - i' - 1) + 2^l - 1 \right], \quad (\text{B2})
\end{aligned}$$

where $i_{<} (i_{>})$ is the greater (lesser) of i and i' .

The integrals in (27)–(29) are

$$J_1 = \int_{-1}^1 dx \, x n(x) [\Theta(1-|y|) y n]_{y=\bar{\varepsilon}_i^{v'} - \bar{\varepsilon}_i^{v'} - x}, \quad (\text{B3})$$

$$\begin{aligned}
J_2 &= \int_{-1}^1 dx \frac{\bar{\varepsilon}_i^{v'} - \bar{\varepsilon}_j^u - x}{(\bar{\varepsilon}_i^{v'} - \bar{\varepsilon}_j^u - x)^2 + \sigma_{ju}^2} x n(x) \\
&\times [\Theta(1-|y|) y n(y)]_{y=\bar{\varepsilon}_i^{v'} - \bar{\varepsilon}_i^{v'} - x}, \quad (\text{B4})
\end{aligned}$$

and

$$\begin{aligned}
J_3 &= \int_{-1}^1 dx \left[P_{ju, j'u} (\bar{\varepsilon}_i^{v'} - \bar{\varepsilon}_j^u - x, \bar{\varepsilon}_i^{v'} - \bar{\varepsilon}_j^u - x) \right. \\
&\quad \left. + P_{ju, j'u} (\bar{\varepsilon}_i^{v'} - \bar{\varepsilon}_j^u - x, \bar{\varepsilon}_i^v - \bar{\varepsilon}_j^u + x) \right] \\
&\times x n(x) [\Theta(1-|y|) y n(y)]_{y=\bar{\varepsilon}_i^{v'} - \bar{\varepsilon}_i^{v'} - x} \quad (\text{B5})
\end{aligned}$$

with

$$P_{iv, i'v'}(x, y) = \frac{xy + \sigma_{i'v'} \sigma_{iv}}{(x^2 + \sigma_{iv}^2)(y^2 + \sigma_{i'v'}^2)}. \quad (\text{B6})$$

In the above, all frequencies have been scaled by the Debye frequency:

$$\bar{\varepsilon}_i^v = \varepsilon_i^v / \omega_D, \quad \sigma_{iv} = -\frac{1}{\omega_D} \text{Re}\Sigma_{iv}(\varepsilon_i^v). \quad (\text{B7})$$

APPENDIX C

The matrix elements of the Morse surface potential and harmonic vibrational oscillator are contained in the functions $H^{(n)}$ that appear in (36) and are defined below:

$$H_{j'u'ju'}^{(1)} = \begin{pmatrix} u \\ v \end{pmatrix}^{1/2} \begin{pmatrix} u' \\ v' \end{pmatrix}^{1/2} \frac{a^{(|u-v| + |u'-v'|)/2}}{|u-v|! |u'-v'|!} G_{j'u'ju'} G_{j'u'ju'} (\sqrt{v'+1} \delta_{u,v'+1} - \sqrt{v'} \delta_{u,v'-1}) (\sqrt{v'+1} \delta_{u',v'+1} - \sqrt{v'} \delta_{u',v'-1}), \quad (C1)$$

$$H_{juju'}^{(2)} = \begin{pmatrix} u \\ v' \end{pmatrix}^{1/2} \begin{pmatrix} u' \\ v' \end{pmatrix}^{1/2} \frac{a^{(|v'-v| + |v'-u'|)/2}}{|v'-u|! |v'-u'|!} G_{j'v'ju'} G_{j'v'ju'} (\sqrt{v+1} \delta_{u,v+1} - \sqrt{v} \delta_{u,v-1}) (\sqrt{v+1} \delta_{u',v+1} - \sqrt{v} \delta_{u',v-1}), \quad (C2)$$

$$H_{j'u'ju'}^{(3)} = -2 \begin{pmatrix} u \\ v \end{pmatrix}^{1/2} \begin{pmatrix} u' \\ v' \end{pmatrix}^{1/2} \frac{a^{(|u-v| + |v'-u'|)/2}}{|u-v|! |v'-u'|!} G_{j'u'ju'} G_{j'v'ju'} (\sqrt{v'+1} \delta_{u,v'+1} - \sqrt{v'} \delta_{u,v'-1}) (\sqrt{v+1} \delta_{u',v+1} - \sqrt{v} \delta_{u',v-1}), \quad (C3)$$

where

$$\begin{pmatrix} v \\ v' \end{pmatrix} = \frac{v_{>}!}{v_{<}!}$$

with $v_{>}$ ($v_{<}$) equal to the maximum (minimum) of (v, v') . $G_{j'v'ju'}$ is given in (B1).

-
- 1T. J. Chuang, Surf. Sci. Rep. **3**, 1 (1983).
 2J. Heidberg, H. Stein, E. Riehl, and A. Nestmann, Z. Phys. Chem. (Neue Folge) **121**, 145 (1980).
 3J. Heidberg, H. Stein, Z. Szilagy, and H. Weiss, Surf. Sci. **158**, 553 (1985).
 4J. Heidberg, H. Stein, and H. Weiss (unpublished).
 5T. J. Chuang, J. Chem. Phys. **76**, 3828 (1982).
 6T. J. Chuang and H. Seki, Phys. Rev. Lett. **49**, 382 (1982).
 7T. J. Chuang, H. Seki, and I. Hussla, Surf. Sci. **158**, 525 (1985).
 8B. Fain and S. H. Lin, Surf. Sci. **147**, 497 (1984).
 9G. S. Wu, B. Fain, A. R. Ziv, and S. H. Lin, Surf. Sci. **147**, 537 (1984).
 10F. G. Celii, M. P. Casassa, and K. C. Janda, Surf. Sci. **141**, 159 (1984).
 11P. Piercy, Z. W. Gortel, and H. J. Kreuzer, in *Advances in Multiphoton Processes and Spectroscopy*, edited by S. H. Lin (World Scientific, Singapore, 1987), Vol. 3, p. 103.
 12Z. W. Gortel, H. J. Kreuzer, P. Piercy, and R. Teshima, Phys. Rev. B **27**, 5066 (1983).
 13Z. W. Gortel, P. Piercy, R. Teshima, and H. J. Kreuzer, Surf. Sci. **166**, L119 (1986).
 14Z. W. Gortel, P. Piercy, R. Teshima, and H. J. Kreuzer, Surf. Sci. **165**, L12 (1986).
 15Z. W. Gortel, H. J. Kreuzer, P. Piercy, and R. Teshima, Phys. Rev. B **28**, 2119 (1983).
 16I. Hussla, H. Seki, Z. W. Gortel, H. J. Kreuzer, and P. Piercy, Phys. Rev. B **32**, 3489 (1985).
 17B. Fain and S. H. Lin, Chem. Phys. Lett. **114**, 497 (1985).
 18Z. W. Gortel, P. Piercy, and H. J. Kreuzer, Surf. Sci. **179**, 176 (1987).
 19B. Bendow and S. C. Ying, Phys. Rev. B **7**, 622 (1973); **7**, 637 (1973).
 20Z. W. Gortel, H. J. Kreuzer, and R. Teshima, Phys. Rev. B **22**, 512 (1980).
 21C. Jedrzejek, K. F. Freed, S. Efrima, and H. Metiu, Chem. Phys. Lett. **79**, 227 (1981).
 22J. Heidberg, H. Stein, and I. Hussla, Surf. Sci. **162**, 470 (1985).
 23C. Jedrzejek, J. Vac. Sci. Technol. (to be published).
 24J. W. Gadzuk and A. C. Lunz, Surf. Sci. **144**, 429 (1984).
 25B. N. J. Persson and M. Persson, Solid State Commun. **36**, 175 (1980).
 26B. N. J. Persson and R. Ryberg, Phys. Rev. Lett. **54**, 2119 (1985).
 27B. N. J. Persson and R. Ryberg, Phys. Rev. B **24**, 6954 (1981).
 28F. M. Hoffman, Surf. Sci. Rep. **3**, 107 (1983).
 29Z. W. Gortel, H. J. Kreuzer, and R. Teshima, Phys. Rev. B **22**, 5655 (1980).
 30J. D. Jackson, *Classical Electrodynamics*, 2nd ed. (John Wiley, New York, 1975).
 31E. Goldys, Z. W. Gortel, and H. J. Kreuzer, Surf. Sci. **116**, 33 (1982).
 32A. Messiah, *Quantum Mechanics* (Wiley, New York, 1963); Vol. 2.
 33H. Umezawa, H. Matsumoto, and M. Tachiki, *Thermo Field Dynamics and Condensed States* (North-Holland, Amsterdam, 1982).
 34A. L. Fetter and J. D. Walecka, *Quantum Theory of Many-Particle Systems* (McGraw-Hill, New York, 1971).
 35W. Heitler, *Quantum Theory of Radiation*, 3rd ed. (Clarendon, Oxford, 1954).
 36J. Heidberg, I. Hussla, and A. Szilagy, J. Electron. Spectrosc. Relat. Phenom. **30**, 53 (1983).
 37S. H. Lin, Y. Fujimura, H. J. Neusser, and E. W. Schlag, *Multiphoton Spectroscopy of Molecules* (Academic, London, 1984).
 38M. Sargent III, M. O. Scully, and W. E. Lamb, Jr., *Laser Physics* (Addison-Wesley, Reading, MA, 1974).
 39T. L. Hill, J. Theor. Biol. **10**, 442 (1966).
 40T. L. Hill, *Thermodynamics for Chemists and Biologists* (Addison-Wesley, Reading, MA, 1968).
 41V. A. Apkarian and E. Weitz, J. Chem. Phys. **76**, 5796 (1982).
 42S. M. Freund, G. Duxbury, M. Röhmed, J. T. Tiedje, and T. Oka, J. Mol. Spectrosc. **52**, 38 (1974).
 43M. P. Casassa, E. H. Heilweil, J. C. Stephenson, and R. R. Cavanagh, J. Vac. Sci. Technol. A **3**, 1655 (1985).